



Full Length Article

High Speed *In-situ* X-ray Imaging of 3D Freeze Printing of AerogelsHalil Tetik^a, Guang Yang^a, Wenda Tan^b, Anthony Fong^c, Shuting Lei^a, Johanna Nelson Weker^{c,*}, Dong Lin^{a,*}^a Department of Industrial and Manufacturing Systems Engineering, Kansas State University, Manhattan, KS, 66506, USA^b Department of Mechanical Engineering, The University of Utah, Salt Lake City, UT, 84112, USA^c Stanford Synchrotron Radiation Lightsources, SLAC National Accelerator Laboratory, Menlo Park, CA, 94025, USA

ARTICLE INFO

Keywords:

3D freeze printing
 High speed *in-situ* X-ray imaging
 Additive manufacturing of aerogel
 Freeze casting
 Drop-on-demand printing

ABSTRACT

3D freeze printing (3DFP) combines drop-on-demand (DOD) inkjet printing with freeze casting to fabricate lightweight and multifunctional aerogels with customized geometries. Freeze casting is an efficient and easily implemented method capable of fabricating porous, sponge-like structures for many different applications. This process enables tailoring the microstructure of the final product (i.e., pore morphology, alignment, average size distribution, etc.) by controlling the fabrication conditions and freezing kinetics. Its combination with DOD printing provides the capability of engineering the macrostructure without relying on a mold as reported for 3D freeze-printed aerogels made from graphene, silver nanowires, and other nanocomposites. In this paper, we performed *in-situ* X-ray imaging to understand the inside process dynamics in 3DFP using a commercially available colloidal silica ink. We investigated the 3DFP process with the following hierarchy: first, single droplets; then, uniform lines obtained from coalescence of droplets; and finally, three consecutive lines deposited layer by layer. With the help of X-ray imaging, the importance of the balance between material deposition and freezing rates was shown *in-situ* by the observation inside of the freeze front following the tip of the printed line. The effects of the substrate temperature on the elimination of undesired interfacial boundaries were also shown by the observed ice crystals penetrating from lower to upper layer.

1. Introduction

Aerogels are gels in which the liquid phase has been replaced by air without significant shrinkage and collapse in the microstructure [1]. They exhibit unique properties such as ultra-low density, high and tunable porosity, large surface area, low thermal conductivity, refractive index, and dielectric constant, which makes them suitable for many different applications [2–5]. Replacement of the liquid by air is achieved through several methods including supercritical fluid drying, solvent-replaced ambient drying, surface-modified ambient drying, freeze drying, and so on [2]. Among these, freeze drying is utilized by a freeze-casting method, which is a well-established process for fabricating aerogels from ceramics [6–10], metals [11–15], carbon-based materials [16–18], nanocomposites [19–22], etc. for many different applications such as energy storage and conversion [23–25], photo catalysis [26], liquid chromatography [27], sensors [28–30], and bioengineering [31,32]. Advantages of freeze casting include but are not limited to its simple procedure, environmental-friendly nature, and ability to tailor the micro structure of the final product [33]. In freeze casting, the precursor, which is composed of a liquid solvent and solute

particles, is frozen inside a mold to provide the desired shape (Fig. 1a). Then solidified solvent crystals are sublimated under low pressure and temperature conditions [34–37]. During freezing, the solute particles are rejected by growing crystals of solvent, which results in a tightly packed network of solute particles (Fig. 1b). Once the solvent crystals are sublimated by freeze drying, a porous structure whose morphology is a replica of the solvent crystals is obtained [34]. Growth of the solvent crystals can be oriented with an applied-temperature gradient as seen in unidirectional and bidirectional freeze casting [38]. Many factors can be used to tailor the microstructure of the freeze-casted aerogels such as size of the solute particles, solid loading of the precursor, type and concentration of the additives used, freezing rate, rheology of the liquid precursor, etc [39–41]. Even though freeze casting has many ways to manipulate the microstructure of the final product, the macrostructure relies heavily on the geometry of the mold used during the process.

Our group has recently developed a 3D freeze-printing (3DFP) process with our collaborators, which is a novel method of combining unidirectional freeze casting with DOD printing to eliminate the need for a mold and increase the customization capabilities of the freeze

* Corresponding authors.

E-mail addresses: jnelson@slac.stanford.edu (J. Nelson Weker), dongl@ksu.edu (D. Lin).<https://doi.org/10.1016/j.addma.2020.101513>

Received 2 May 2020; Received in revised form 27 July 2020; Accepted 2 August 2020

Available online 10 August 2020

2214-8604/ © 2020 Elsevier B.V. All rights reserved.

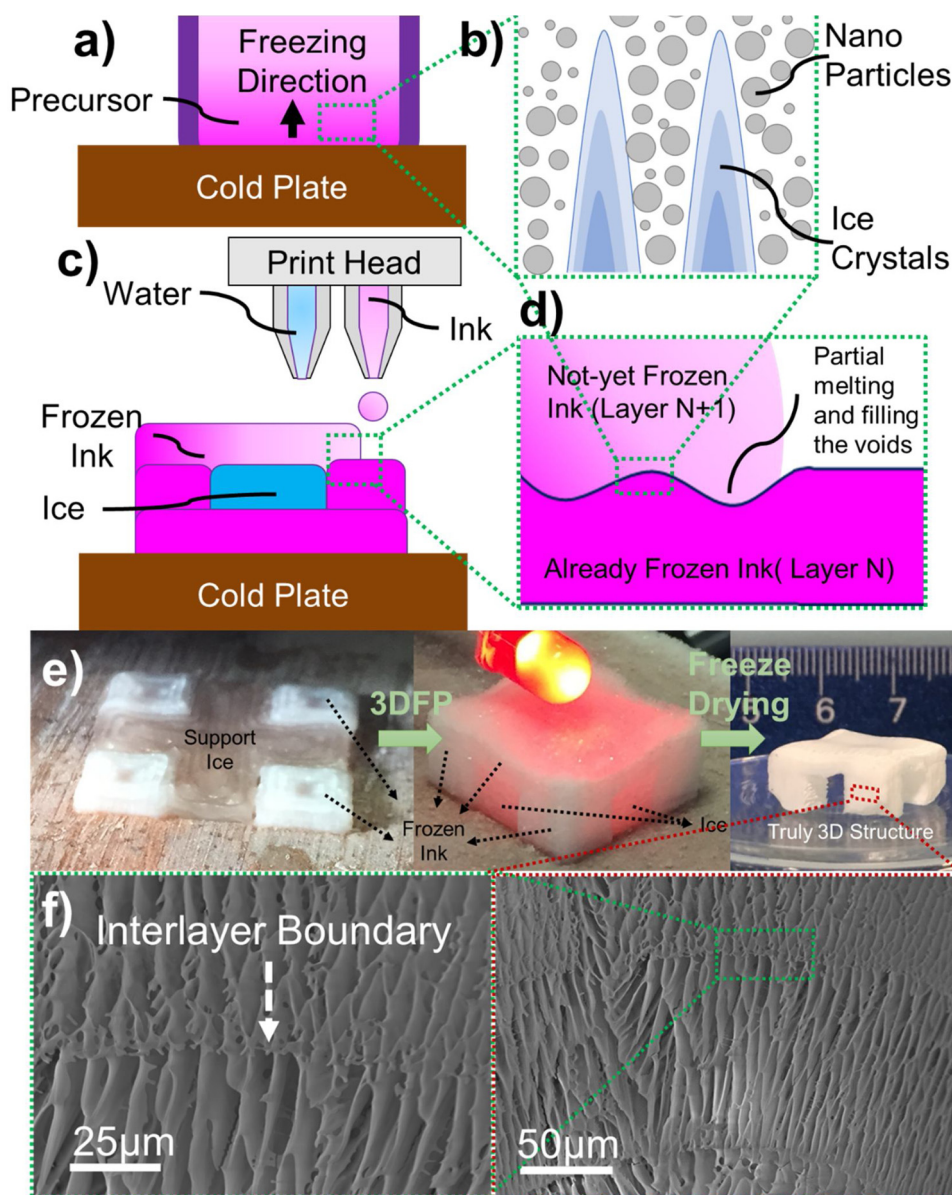


Fig. 1. a) Schematics of the unidirectional freeze casting process. b) Growth of ice crystals along the temperature gradient in directional freezing process. c) Schematics of the 3DFP processes using water as support material to fabricate 3D structures with overhang features. d) Schematics illustrating the partial melting that already frozen ink (N^{th} layer) experiences after depositing liquid ink ($N+1^{\text{th}}$ layer) on top of it. e) 3DFP of a truly 3D structure from SiO_2 -PVA ink using water as support material. f) SEM micrographs showing void-free interfacial boundary obtained by 3DFP process.

casting process [42–45]. With 3DFP, droplets of liquid precursors are generated using a DOD dispenser and are deposited on top of a substrate whose temperature is well below the freezing point of the solvent used in the liquid precursor (Fig. 1c). As droplets have contact with the precooled substrate, the solvents experience an immediate freezing which allows them to preserve their shape. With the reduced distance and time between separate droplets, uniform lines can be obtained after the coalescence of droplets. Using these lines, complex 3D frozen structures can be achieved without using a mold. Frozen structures with desired shapes are freeze dried, which sublimates the solvent crystals, and a porous aerogel is obtained. Since 3DFP involves freeze casting, the micro-structure of the final aerogel can be manipulated by the freezing kinetics. As in the unidirectional freeze-casting process, solvent crystals grow from bottom to top along the temperature gradient (Fig. 1b) and controlling the substrate temperature offers control of the average pore-size distribution. Additives that will not affect the printability of the precursor can be used for manipulating the solvent crystal

morphology. Besides its ability to tailor the microstructure of the final aerogel, 3DFP is also capable of fabricating true 3D structures with overhang features by using water as support material (Fig. 1c). Deposited ink at room temperature ($N+1^{\text{th}}$ layer - Fig. 1d) causes a partial melting on top of the previously deposited and frozen ink (N^{th} layer - Fig. 1d). Since the ink's viscosity is low, it fills the possible voids that could occur between layers by the help of surface tension and gravitational forces. And finally, partially melted part of N^{th} layer fuses with the not yet frozen $N+1^{\text{th}}$ layer and they both freeze together. This eliminates insufficient bonding, interfacial boundaries, and voids between layers and yields aerogels with ultralow densities. To demonstrate the capabilities of the 3DFP process, we fabricated an aerogel with overhang feature as given in Fig. 1e. More details can be found in our previous publication on 3D printing of graphene aerogels with overhang features [45]. Once 3DFP process is completed, supporting ice is completely sublimated with the following freeze drying process. The micrographs show the alignment of the pores along the freezing

direction (from bottom to top) as well as the void-free interfacial boundaries, which two of the most important advantages of the 3DFP process.

Freeze-casting processes have widely been investigated *in-situ* using optical [46–49] and X-ray [50–53] imaging systems to identify unknown aspects of the process. However, X-ray imaging, which is one of the most informative methods to investigate the morphology of freeze-casted structures [50], provides some advantages over optical imaging methods. These advantages include elimination of the requirement to use optically transparent materials, ability to observe inside of the material, eliminating the need for suspensions composed of single and large particles to provide clearer observations, and higher spatial resolution [52–54]. Therefore, X-ray imaging techniques have been used to investigate the process dynamics of several 3D printing processes including laser powder-bed fusion [55–59], powder-blown laser-additive manufacturing [60], and binder jetting-additive manufacturing [61]. Since 3DFP is a hybrid process in which DOD printing was followed by freeze drying and a subsequent heat treatment (when required), investigation of final products thereafter the complete process does not provide quality information regarding the “3DFP” part of the process, which plays a crucial role in the product quality. To understand the relation between substrate temperature, which controls the freezing rate of the deposited material, and deposition rate of the material, and the ice crystal growth mechanism along the interfacial boundaries, which ensures a good fusion of subsequent layers, we performed the *in-situ* investigation of the process using X-ray imaging techniques. Using the setup given in Fig. 2, we performed *in-situ* X-ray imaging of separate droplets, lines obtained after coalescence of droplets and three consecutive lines deposited layer by layer. We showed that achieving uniform lines from separate droplets depends on a careful balance between material deposition and freezing (solidification) rates. With the advantages provided by the X-ray imaging techniques, we were able to observe freeze front, deposited material, and growing ice crystals simultaneously. To the best of our knowledge, this is the first study reporting an *in-situ* X-ray imaging experiment investigating material deposition and freezing processes simultaneously.

2. Materials and Methods

2.1. Materials

For the *in-situ* X-ray imaging experiments, a 15 wt. % colloidal silica suspension with an average particle size of 4–6 nm (Nyacol, MA, USA)

was used as ink. Schematics of the 3D freeze printing setup is given in Fig. 2. Briefly, a three-axis motion stage (Panowin Technologies, Shanghai, China) was used to manipulate the DOD print-head, which was composed of a syringe barrel (Nordson EFD, RI, USA) and a solenoid micro dispenser (The Lee Co, CT, USA) loaded with a nozzle tip having a diameter of 190 μm . Solenoid micro dispensers operate through an internal piston, which forces the valve to open and close via an induced magnetic field [62]. Once the piston is actuated and the valve is opened, pressurized ink moves to the orifice and is ejected as droplets [63]. An electrical pulse, whose length determines the opening time of the valve, is used to actuate the piston that allows or blocks ink flow [64,65]. A pneumatic fluid dispenser (Nordson EFD, RI, USA) was used to control the pressure inside the syringe barrel. Solenoid micro dispenser was used to generate fine droplets of colloidal silica ink with desired jetting frequencies. A liquid-nitrogen (L-N_2)-operated hot/cold plate (Instec, CO, USA) was used to control the temperature of the substrate.

2.2. Methods

In-situ investigation of the 3DFP process using white light synchrotron X-rays was performed at bending magnet beamline 2–2 of Stanford Synchrotron Radiation Lightsource, SLAC National Accelerator Laboratory in CA, USA. Using the setup given in Fig. 2, the material was deposited along y axis for 10 mm, at a single x coordinate. By tuning the print-head speed and jetting frequency, we performed the material deposition as separate droplets, uniform lines obtained after coalescence of droplets, and three consecutive lines deposited layer by layer (Fig. 2). The image of the deposited material, which was hit by the X-ray, was recorded by a camera chip. By adjusting the DOD print-head speed and jetting frequency, we controlled the distance between the successive droplets and investigated the freezing process of separate droplets, as well as single layer uniform lines and three consecutive lines deposited layer by layer.

X-ray images were collected using a scintillator-based optical system with a 100 μm YAG:Ce scintillator crystal (Crytur Ltd.) coated in 120 nm of Al on the upstream side, high reflectance mirror (Thorlabs) to bend the visible light 90° off-axis to the X-rays into a 4x long working distance infinity corrected objective lens (Nikon), infinity-corrected tube lens (Thorlabs), and high speed CMOS camera pco.dimax S4 (PCO). With these optical components, the effective pixel size is 2.4 μm for a field of view of 4.8 mm x 2.4 mm and images were captured at 500 Hz. The stroboscopic images showing the droplet-generation process

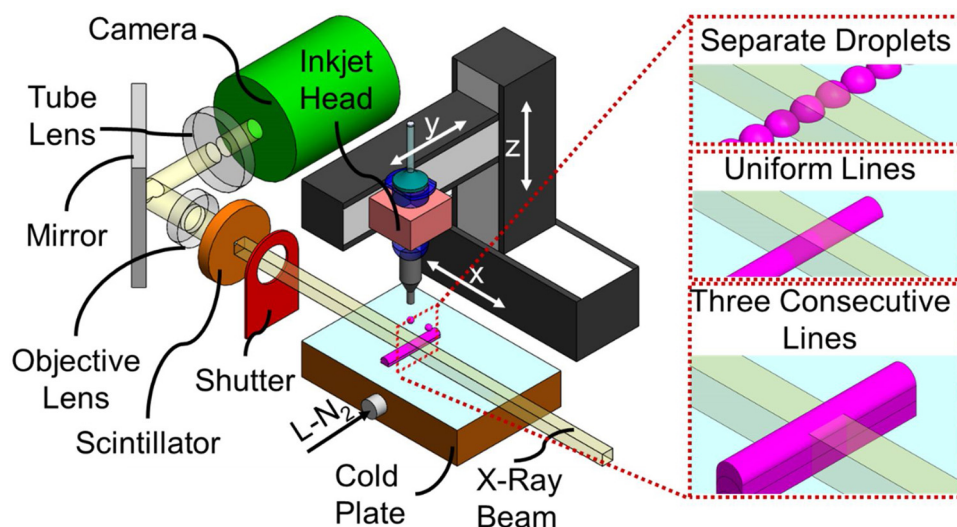


Fig. 2. Schematics of the experimental setup used in the synchrotron radiation light source facility and deposited structures (separate droplets, uniform lines, and three consecutive lines deposited layer by layer) investigated *in-situ*.

were obtained using a CCD camera (Sentech) synchronized with an LED bulb.

Images showing the top view of deposited material (Fig. 5) were obtained using an optical microscope (Olympus). Samples in these images were prepared by depositing the colloidal silica ink on top of a silicon wafer substrate at given temperatures. 3D freeze printed samples demonstrated in Fig. 1e were fabricated after adding a weighted amount of PVA into the colloidal silica ink used in *in-situ* experiments since colloidal silica requires additional binding agents and further sintering after 3DFP to protect the structural integrity of the aerogels [52]. 3D freeze printed samples were treated by a subsequent freeze drying process for 48 h where the temperature was $-35\text{ }^{\circ}\text{C}$ and the pressure was 0.2 mbar.

3. Results and Discussion

3.1. *In-situ* investigation of single droplets

3DFP employs a DOD printing system for several reasons. DOD printing generates droplets of low-concentration inks that yield aerogels with ultra-low densities. It can use water as a supporting material to fabricate true 3D structures with overhang structures. Ability of low viscosity inks to fill the voids under surface tension and gravity eliminates voids and insufficient bonding between subsequent layers unlike most of other traditional 3D printing methods [45]. The rheological requirements for printability of an ink are determined by Reynolds, Weber, and Ohnesorge numbers, which are dimensionless numbers related to the physical properties of the ink such as viscosity, surface tension, and density [66–69]. A solenoid micro dispenser was employed in this study due to its robustness and allowing more flexibility for the ink formulation and process [70]. After adjusting the pressure of the ink, opening time of the solenoid micro dispenser, and diameter of the nozzle tip, we generated satellite-free droplets from the colloidal silica ink as presented with the stroboscopic optical images given in Fig. 3a. The stroboscopic images were taken by a CCD camera with a 30-fps frame rate and a strobed LED behind the droplets. To freeze the droplet images and capture different phases of the droplet-generation process, we used various delay times between the drop ejection and LED strobe. The diameter of the spherical droplets was measured as approximately $d_0 \cong 190\text{ }\mu\text{m}$, which is approximately equal to the diameter of the nozzle tip used for the experiments. The volume of the ejected droplets was calculated as approximately $\sim 3.6\text{ nL}$.

Van Dam and Clerc [71] proposed to model the deposited droplets as spherical caps, schematically explained in Fig. 3b. This spherical cap has a height of h , bead width of w , polar angle of θ , and radius of r .

Considering a volumetric conservation, the volume of the spherical droplet before the deposition should be equal to the volume of the spherical cap right after the deposition. Following the deposit of the generated droplet on the substrate, we measured the dimensions of five adjacent droplets and calculated the average dimensions of the spherical cap as $w = 380.78\text{ }\mu\text{m}$, and $h = 59.98\text{ }\mu\text{m}$, where h is the height of the spherical cap after it had been deposited (before formation of the conical tip). Measured dimensions of the spherical cap correspond to an initial volume of $V = (\pi h/6)(3(w/2)^2 + h^2) = 3.59\text{ nL}$, which is consistent in terms of volumetric conservation.

However, Van Dam and Clerc's spherical cap model does not consider a phase change after the deposition. It has been shown that when droplets of water are deposited on a cold plate, a conical tip is formed as the freeze front reaches to the top of the droplet [72–74] (as shown in Fig. 3c). This transformation of the droplet shape is attributed to the thermal expansion that water experiences after freezing [73]. Since the colloidal silica suspension we used for the experiments is water-based, we also observed a shape change and a volumetric expansion in the droplets after complete freezing. As seen in Fig. 3d and the supporting information Video S1, at the instant a droplet was deposited on the substrate, it had a spherical cap shape. As the time passed and the droplet froze, it experienced a thermal expansion and a conical tip formed at the top (pointed with the red arrow in Fig. 3d). Using the *in-situ* X-ray images we obtained, we measured the bead width (w) and height (h) of five different droplets along the freezing process. To reduce the noise in the raw images, we processed them and increased their contrasts so that the distinction between the droplets and their surroundings is clear (Fig. 3d). Measurements were done using ImageJ software by defining a pixel to μm scale ratio (0.42 pixels/ μm), manually drawing lines along the width/height of the droplets and recoding the corresponding dimensions. We measured the dimensions of five consecutive droplets from the initial frame at which the droplet was deposited ($t = 0\text{ s}$) to the final frame at which the droplet reached to its maximum height value ($t = 0.14\text{ s}$). Average values of the dimensions for five different droplets are provided in Fig. 3e. We observed the average value of the bead width (w) value remained closed to an average value of $380.78\text{ }\mu\text{m}$, while the average height of the droplets increased from $59.9\text{ }\mu\text{m}$ to $79.9\text{ }\mu\text{m}$, which corresponds to an increase of $\Delta h = 33.4\%$. We used the amount of increase in the height of droplets after complete freezing to estimate the height of a line in the next subsection.

3.2. *In-situ* X-ray investigation of line formation

In order to achieve aerogels with complex 3D geometries, separate

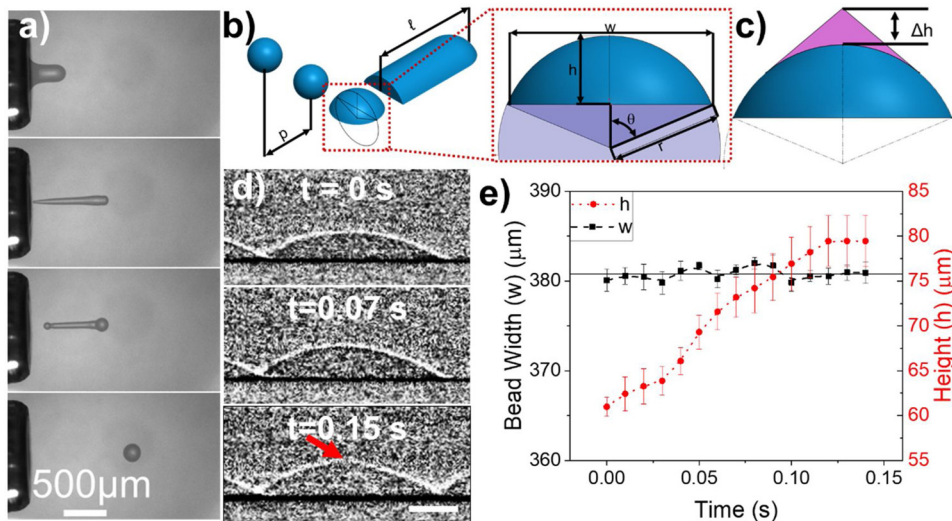


Fig. 3. a) Stroboscopic optical images showing the phases of droplet formation process using colloidal silica ink without any satellite formation. b) Schematics of a single droplet (before and after impact) and formed line after coalescence of multiple droplets. c) Schematics of a single droplet after experiencing the thermal expansion leading to formation of a conical tip on top of the spherical cap shape. d) *In-situ* X-ray images showing growth of conical tip on top of the spherical cap shaped droplet after experiencing a thermal expansion. The scale bar is $100\text{ }\mu\text{m}$. e) The change in the dimensions of a single droplet due to thermal expansion.

droplets need to coalesce so they can form a continuous line to build 3D geometries. Obtaining continuous lines depends on a well-adjusted balance between print-head speed (v), jetting frequency (f), and the diameter of the droplet before impact (d_0). The pitch distance between successive droplets is a function of the jetting frequency and print-head speed ($p = v/f$). The geometry of these continuous lines can be modelled as beads with a constant cross section of a circular segment as proposed by Stringer and Derby [75]. Assuming a uniform line with a length of ℓ as given in Fig. 3b, and considering volumetric conservation, total volume of the deposited droplets is equal to the volume of the line with constant cross section of a circular segment:

$$N \left(\frac{\pi}{6} d_0^3 \right) = \left(r^2 \theta - \frac{wr \cos \theta}{2} \right) \ell \quad (1)$$

where N is the number of droplets required for the length of $\ell = pN$, $r = ((w/2)^2 + h^2)/2h$, and $\theta = \sin^{-1}(w/2r)$. The left-hand side of Eq. (1) corresponds to the total volume of spherical droplets with the quantity of N . The right-hand side corresponds to the volume of a line having the cross-section of a spherical cap, which would be obtained without any phase change due to freezing. Eq. (1) can be solved for h , with given d_0 and w , which will not include the thermal expansion in the calculation observed after freezing. To take it into account, we added a correction factor of $c = 1.334$, which corresponds to an average increase of 33.4% in the height of single droplets after freezing. It was found by calculating the mean of measured increase in the height of five successive droplets. By multiplying the obtained height from Eq. (1) with the correction factor, we were able to estimate the height of lines obtained after coalescence of droplets with different pitch distances. In order to validate this theory, we printed lines with different pitch distances (Fig. 4a) and their height were measured (Fig. 4b). The estimated values for the line heights with and without the correction factor were also provided in the plot, which shows that including the correction factor in the estimation of line heights provides a better agreement with the measured heights. This showed us that the geometrical model of Stringer and Derby for a line obtained after coalescence of droplets can be used to model the geometry of the 3D freeze printed lines after considering a correction factor due to the thermal expansion of water. Measurements of the line height with different pitch-distance values were performed using the X-ray images (Fig. 4a), which were obtained using a print-head speed of $v = 10 \text{ mm.s}^{-1}$.

In the 3DFP process, uniformity of a line fabricated by coalescence of multiple droplets not only depends on the pitch distance, but also the time between two successive droplets (τ). Because droplets experience rapid solidification after impact, τ must be short enough to provide liquid-to-liquid interaction between adjacent droplets to achieve coalescence. Accordingly, Mingirulli et al., previously showed that molten wax deposited by a DOD dispenser cannot achieve a smooth

coalescence when τ is too high. Instead of continuous uniform lines, they observed each droplet separately solidified (frozen) [76]. Furthermore, Sukhotskiy et al., reported a simulation study for molten-metal DOD printing, showing adjacent droplets cannot achieve a smooth coalescence as the time between the impact of successive droplets increases by reducing the jetting frequency, even though the inter-droplet pitch distance is kept the same [77]. To show the effects of different τ on the morphology of the printed lines, we fabricated lines with different print-head speeds (Fig. 5). Fig. 5a presents side- and top-view images of the deposited droplets obtained by *in-situ* X-ray imaging and optical microscopy, respectively. In this figure, the print-head speed was $v = 1 \text{ mm.s}^{-1}$ and the jetting frequency was $f = 4 \text{ Hz}$, which yields a pitch distance of $p = 250 \mu\text{m}$ and an inter-droplet duration of $\tau = 250 \text{ ms}$. In this configuration the earlier droplet was fully solidified before the deposition of the adjacent droplet. However, when the print-head speed was increased to $v = 10 \text{ mm.s}^{-1}$, using the same pitch distance ($f = 40 \text{ Hz}$, $p = 250 \mu\text{m}$, and $\tau = 25 \text{ ms}$), time lapse was short enough for the droplets to achieve coalescence before the complete solidification of the previous droplet (Fig. 5b). To better visualize the coalescence of separate droplets under the effect of freezing, we decreased the pitch distance to $p = 75 \mu\text{m}$ and observed the freezing. When time and distance between two successive droplets are appropriate, the freeze front is observed before the tip of the line printed and a uniform line is formed after coalescence of separate droplets (Fig. 5c and supporting information Video S2).

3.3. *In-situ* X-ray investigation of three consecutive lines

One of the main advantages of 3DFP is its ability to use low-viscosity inks which instantly fill the possible voids between layers observed in most of other 3D-printing techniques under surface tension and gravity such as extrusion-based 3D printing. Furthermore, when liquid suspension is deposited on top of a previously frozen layer, the not-yet-frozen material melts the already-frozen surface. These two materials (previously frozen and not-yet frozen) are mixed and refreeze together [45]. To understand the fusion of subsequent layers and ice crystal growing mechanism along the interfacial boundaries, we deposited three consecutive lines layer by layer and investigated the interfacial regions *in-situ* using X-ray (Fig. 6). The print-head speed in these experiments was $v = 10 \text{ mm.s}^{-1}$, the pitch distance was $p = 100 \mu\text{m}$. When the substrate temperature was set to $T_{\text{subs}} = -30^\circ\text{C}$, the rate of freezing was fast enough for the deposited ink to preserve the shape, and slow enough to allow filling of voids for a sufficient interfacial bonding. There is no visible void or interfacial boundary exists between consecutive layers (Fig. 6a). Furthermore, ice crystals that grew during the freezing were visible in the X-ray images. It was observed that those ice crystals penetrate from the second layer to the

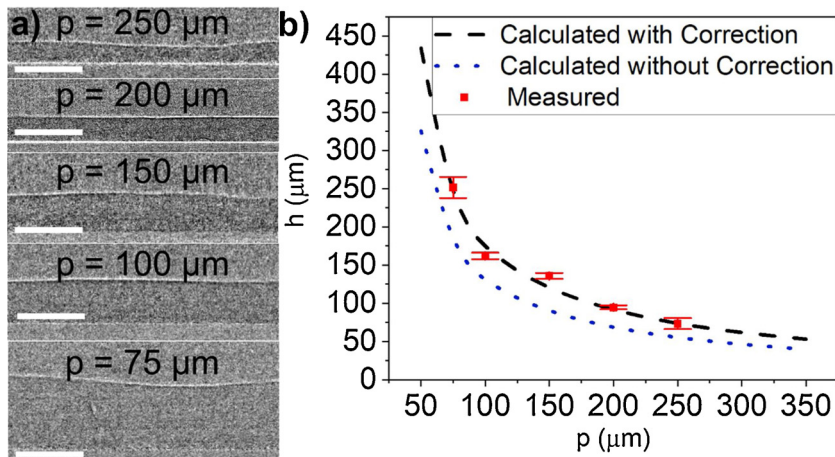


Fig. 4. a) Formation of lines after successive deposition of droplets with different pitch distances. The print head speed for all pitch distances is 10 mm.s^{-1} . The scale bar is $250 \mu\text{m}$. b) Comparison of calculated (with and without correction factor due to thermal expansion and shape change) and measured values of the layer heights as a function of pitch distance.

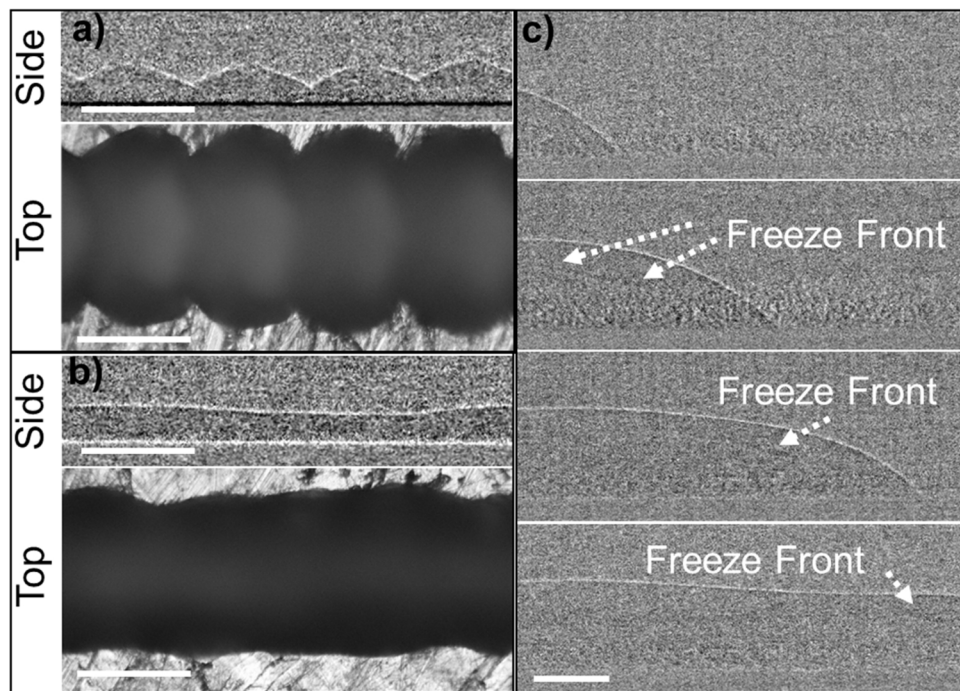


Fig. 5. Investigation of line-formation process using a constant pitch distance of 250 μm and a print head speed of a) 1 $\text{mm}\cdot\text{s}^{-1}$ and b) 10 $\text{mm}\cdot\text{s}^{-1}$. Side view images were obtained using *in-situ* X-ray, and top view images were obtained using an optical microscope after freeze dyeing of the deposited lines. c) X-ray images obtained *in-situ* showing a good relationship between the freeze-front velocity and print head speed. The print head speed in this figure is 10 $\text{mm}\cdot\text{s}^{-1}$ and the pitch distance is 75 μm . All scale bars are 250 μm .

third layer without any formation of a visible boundary (Fig. 6b and supporting information Video S3). This penetration generates interconnected pores in the printed layers. This demonstrates that when the required conditions (e.g., substrate temperature, environment temperature, and relative humidity) are supplied, 3DFP is capable of eliminating the interfacial boundaries observed in most of the 3D-printing techniques. When the substrate temperature was reduced to $T_{\text{subs}} = -70^\circ\text{C}$ (Fig. 6c), the rate of freezing increased tremendously and the deposited ink did not have enough time to fill the voids before completely solidifying. This yielded to formation of interfacial boundaries between consecutive layers, which were possible to detect using *in-situ* X-ray images.

4. Conclusion

3DFP is a method used for fabricating customized aerogels for different applications including supercapacitor electrodes, sodium-ion battery anodes, electro-mechanical sensors, flexible electronics, etc. The ability of this printing method on eliminating voids and interfacial boundaries between layers is exceptional when compared to most of other 3D-printing techniques. The other conclusions we have drawn from the experiments can be categorized as follows:

- 1 Dimensions of uniform lines formed after the coalescence of single droplets can be estimated from the droplet volume and measuring just one dimension of the spherical cap (after deposition). Also,

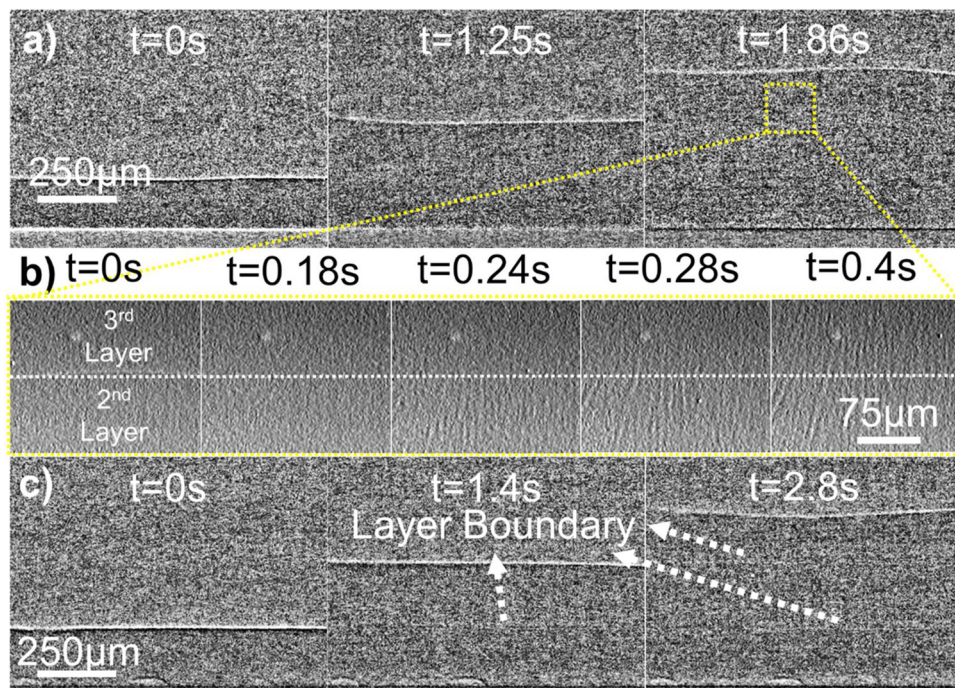


Fig. 6. a) *In-situ* X-ray images showing three consecutive lines deposited layer by layer fabricated with a substrate temperature of -30°C . b) *In-situ* X-ray images showing growth of ice crystals along two consecutive layers when the substrate temperature was -30°C . c) Three consecutive lines deposited layer by layer fabricated with a substrate temperature of -70°C .

since deposited droplets experience a phase change, thermal expansions/retractions should be considered for applying the conservation of volume in order to estimate the dimensions of the formed line.

- 2 Using the 3DFP process, the formation of uniform lines not only depends on the pitch distance between two successive droplets, but also the inter-droplet duration. If the former droplet totally freezes before the later droplet reaches the substrate, there is not enough time for coalescence. To ensure a maximum product quality, a well-adjusted balance between the material deposition and freezing rate must be achieved as confirmed by the *in-situ* observation of the freeze front following the tip of the printed line.
- 3 3DFP provides an exceptional capability of fabricating aerogels without formation of voids and boundaries in between consecutive layers. This is achieved by partial melting of the already-frozen layer and employing low-viscosity inks, which fill the existing voids under surface tension and gravitational forces. *In-situ* experiments showed that ice crystals grow continuously along the interfacial boundaries without allowing any void or boundary formation between consecutive layers confirming the elimination of layer boundaries in 3DFP process.

Author Contribution

Halil Tetik: Design of study, acquisition of data, analysis of data, drafting the manuscript

Guang Yang: Design of study, acquisition of data.

Wenda Tan: Conception, revising the manuscript critically for important intellectual content

Anthony Fong: Acquisition of data.

Shuting Lei: Conception, design of study, revising the manuscript critically for important intellectual content.

Johanna Nelson Weker: Acquisition of data, revising the manuscript critically for important intellectual content.

Dong Lin: Conception, design of study, revising the manuscript critically for important intellectual content.

Declaration of Competing Interest

The authors report no declarations of interest.

Acknowledgements

Prof. Lin acknowledges support from the National Science Foundation under Award No. OIA-1656006 and matching support from the state of Kansas through the Kansas Board of Regents, NASA EPSCoR CAN Grant under Award No. 80NSSC19M0153, and Johnson Cancer Center. Use of the Stanford Synchrotron Radiation Lightsource, SLAC National Accelerator Laboratory, is supported by the U.S. Department of Energy, Office of Science, Office of Basic Energy Sciences under Contract No. DE-AC02-76SF00515.

Appendix A. Supplementary data

Supplementary material related to this article can be found, in the online version, at doi:<https://doi.org/10.1016/j.addma.2020.101513>.

References

- [1] S.S. Kistler, Coherent expanded aerogels and jellies, *Nature* 127 (3211) (1931) p. 741–741.
- [2] A. Du, B. Zhou, Z. Zhang, J. Shen, A special material or a new state of matter: a review and reconsideration of the aerogel, *Materials* 6 (3) (2013) 941–968.
- [3] G. Gorgolis, C. Galiotis, Graphene aerogels: a review, *2D Mater.* 4 (3) (2017) 032001.
- [4] J. Stergar, U. Maver, Review of aerogel-based materials in biomedical applications, *J. Solgel Sci. Technol.* 77 (3) (2016) 738–752.
- [5] T.A. Esquivel-Castro, M. Ibarra-Alonso, J. Oliva, A. Martínez-Luévano, Porous aerogel and core/shell nanoparticles for controlled drug delivery: a review, *Mater. Sci. Eng. C* 96 (2019) 915–940.
- [6] K. Araki, J.W. Halloran, New freeze-casting technique for ceramics with sublimable vehicles, *J. Am. Ceram. Soc.* 87 (10) (2004) 1859–1863.
- [7] S.W. Sofie, F. Dogan, Freeze casting of aqueous alumina slurries with glycerol, *J. Am. Ceram. Soc.* 84 (7) (2001) 1459–1464.
- [8] T. Waschkiess, R. Oberacker, M.J. Hoffmann, Control of lamellae spacing during freeze casting of ceramics using double-side cooling as a novel processing route, *J. Am. Ceram. Soc.* 92 (2009) 579–584.
- [9] J. Han, C. Hong, X. Zhang, J. Du, W. Zhang, Highly porous ZrO₂ ceramics fabricated by a camphene-based freeze-casting route: microstructure and properties, *J. Eur. Ceram. Soc.* 30 (1) (2010) 53–60.
- [10] L. Hu, C.-A. Wang, Y. Huang, C. Sun, S. Lu, Z. Hu, Control of pore channel size during freeze casting of porous YSZ ceramics with unidirectionally aligned channels using different freezing temperatures, *J. Eur. Ceram. Soc.* 30 (16) (2010) 3389–3396.
- [11] H.-D. Jung, S.-W. Yook, H.-E. Kim, Y.-H. Koh, Fabrication of titanium scaffolds with porosity and pore size gradients by sequential freeze casting, *Mater. Lett.* 17 (63) (2009) 1545–1547.
- [12] G. Gouws, N. Shortt, Microstructured silver surfaces produced by freeze casting for enhanced phase change heat transfer, *Journal of Physics: Conference Series*, IOP Publishing, 2015.
- [13] F. Qian, P.C. Lan, M.C. Freyman, W. Chen, T. Kou, T.Y. Olson, C. Zhu, M.A. Worsley, E.B. Duoss, C.M. Spadaccini, Ultralight conductive silver nanowire aerogels, *Nano Lett.* 17 (12) (2017) 7171–7176.
- [14] Y. Tang, K.L. Yeo, Y. Chen, L.W. Yap, W. Xiong, W. Cheng, Ultralow-density copper nanowire aerogel monoliths with tunable mechanical and electrical properties, *J. Mater. Chem. A* 1 (23) (2013) 6723–6726.
- [15] A.I. Ramos, D.C. Dunand, Preparation and characterization of directionally freeze-cast copper foams, *Metals* 2 (3) (2012) 265–273.
- [16] C. Wang, X. Chen, B. Wang, M. Huang, B. Wang, Y. Jiang, R.S. Ruoff, Freeze-casting produces a graphene oxide aerogel with a radial and centrosymmetric structure, *ACS Nano* 12 (6) (2018) 5816–5825.
- [17] W. Gao, N. Zhao, W. Yao, Z. Xu, H. Bai, C. Gao, Effect of flake size on the mechanical properties of graphene aerogels prepared by freeze casting, *RSC Adv.* 7 (53) (2017) 33600–33605.
- [18] J. Bai, Y. Huang, Q. Gong, X. Liu, Y. Li, J. Gan, M. Zhao, Y. Shao, D. Zhuang, J. Liang, Preparation of porous carbon nanotube/carbon composite spheres and their adsorption properties, *Carbon* 137 (2018) 493–501.
- [19] B. Wicklein, A. Kocjan, G. Salazar-Alvarez, F. Carosio, G. Camino, M. Antonietti, L. Bergström, Thermally insulating and fire-retardant lightweight anisotropic foams based on nanocellulose and graphene oxide, *Nat. Nanotechnol.* 10 (3) (2015) 277.
- [20] P.K. Sahoo, N. Kumar, S. Thiyagarajan, D. Thakur, H.S. Panda, Freeze-Casting of multifunctional cellular 3D-graphene/Ag nanocomposites: synergistically affect supercapacitor, catalytic, and antibacterial properties, *ACS Sustain. Chem. Eng.* 6 (6) (2018) 7475–7487.
- [21] S.M.H. Ghazanfari, A. Zamanian, Phase transformation, microstructural and mechanical properties of hydroxyapatite/alumina nanocomposite scaffolds produced by freeze casting, *Ceram. Int.* 39 (8) (2013) 9835–9844.
- [22] W. Li, K. Lu, J.Y. Walz, Formation, Structure and Properties of Freeze-Cast Kaolinite–Silica Nanocomposites, *J. Am. Ceram. Soc.* 94 (4) (2011) 1256–1264.
- [23] C.-C. Ji, M.-W. Xu, S.-J. Bao, C.-J. Cai, Z.-J. Lu, H. Chai, F. Yang, H. Wei, Self-assembly of three-dimensional interconnected graphene-based aerogels and its application in supercapacitors, *J. Colloid Interface Sci.* 407 (2013) 416–424.
- [24] P. Zuo, W. Zhang, J. Hua, Y. Ma, C. Du, X. Cheng, Y. Gao, G. Yin, A novel one-dimensional reduced graphene oxide/sulfur nanoscroll material and its application in lithium sulfur batteries, *Electrochim. Acta* 222 (2016) 1861–1869.
- [25] C. Stolze, T. Janoschka, S. Flauder, F.A. Müller, M.D. Hager, U.S. Schubert, Investigation of ice-templated porous electrodes for application in organic batteries, *ACS Appl. Mater. Interfaces* 8 (36) (2016) 23614–23623.
- [26] C. Suwanchawalit, A.J. Patil, R.K. Kumar, S. Wongnawa, S. Mann, Fabrication of ice-templated macroporous TiO₂-chitosan scaffolds for photocatalytic applications, *J. Mater. Chem.* 19 (44) (2009) 8478–8483.
- [27] M. Barrow, A. Eltmimi, A. Ahmed, P. Myers, H. Zhang, Frozen polymerization for aligned porous structures with enhanced mechanical stability, conductivity, and as stationary phase for HPLC, *J. Mater. Chem.* 22 (23) (2012) 11615–11620.
- [28] J. Kuang, L. Liu, Y. Gao, D. Zhou, Z. Chen, B. Han, Z. Zhang, A hierarchically structured graphene foam and its potential as a large-scale strain-gauge sensor, *Nanoscale* 5 (24) (2013) 12171–12177.
- [29] C. Hou, H. Wang, Q. Zhang, Y. Li, M. Zhu, Highly conductive, flexible, and compressible all-graphene passive electronic skin for sensing human touch, *Adv. Mater.* 26 (29) (2014) 5018–5024.
- [30] J. Kuang, Z. Dai, L. Liu, Z. Yang, M. Jin, Z. Zhang, Synergistic effects from graphene and carbon nanotubes endow ordered hierarchical structure foams with a combination of compressibility, super-elasticity and stability and potential application as pressure sensors, *Nanoscale* 7 (20) (2015) 9252–9260.
- [31] J.J. Campbell, A. Husmann, R.D. Hume, C.J. Watson, R.E. Cameron, Development of three-dimensional collagen scaffolds with controlled architecture for cell migration studies using breast cancer cell lines, *Biomaterials* 114 (2017) 34–43.
- [32] Y. Zhu, K. Song, S. Jiang, J. Chen, L. Tang, S. Li, J. Fan, Y. Wang, J. Zhao, T. Liu, Numerical simulation of mass transfer and three-dimensional fabrication of tissue-engineered cartilages based on chitosan/gelatin hybrid hydrogel scaffold in a rotating bioreactor, *Appl. Biochem. Biotechnol.* 181 (1) (2017) 250–266.
- [33] T. Fukasawa, M. Ando, T. Ohji, S. Kanzaki, Synthesis of porous ceramics with complex pore structure by freeze-dry processing, *J. Am. Ceram. Soc.* 84 (1) (2001)

- 230–232.
- [34] S. Deville, Freeze-casting of porous ceramics: a review of current achievements and issues, *Adv. Eng. Mater.* 10 (3) (2008) 155–169.
- [35] M. Naviroj, S. Miller, P. Colombo, K. Faber, Directionally aligned macroporous SiOC via freeze casting of preceramic polymers, *J. Eur. Ceram. Soc.* 35 (8) (2015) 2225–2232.
- [36] A. Macchetta, I.G. Turner, C.R. Bowen, Fabrication of HA/TCP scaffolds with a graded and porous structure using a camphene-based freeze-casting method, *Acta Biomater.* 5 (4) (2009) 1319–1327.
- [37] R. Dash, Y. Li, A.J. Ragauskas, Cellulose nanowhisker foams by freeze casting, *Carbohydr. Polym.* 88 (2) (2012) 789–792.
- [38] K.L. Scotti, D.C. Dunand, Freeze casting—A review of processing, microstructure and properties via the open data repository, *Freeze Cast. Net. Prog. Mater. Sci.* 94 (2018) 243–305.
- [39] M.M. Porter, R. Imperio, M. Wen, M.A. Meyers, J. McKittrick, Bioinspired scaffolds with varying pore architectures and mechanical properties, *Adv. Funct. Mater.* 24 (14) (2014) 1978–1987.
- [40] L. Yan, J. Wu, L. Zhang, X. Liu, K. Zhou, B. Su, Pore structures and mechanical properties of porous titanium scaffolds by bidirectional freeze casting, *Mater. Sci. Eng. C* 75 (2017) 335–340.
- [41] Y. Zhang, K. Zuo, Y.-P. Zeng, Effects of gelatin addition on the microstructure of freeze-cast porous hydroxyapatite ceramics, *Ceram. Int.* 35 (6) (2009) 2151–2154.
- [42] E. Brown, P. Yan, H. Tekik, A. Elangovan, J. Wang, D. Lin, J. Li, 3D printing of hybrid MoS₂-graphene aerogels as highly porous electrode materials for sodium ion battery anodes, *Mater. Des.* 170 (2019) 107689.
- [43] C. Ma, R. Wang, H. Tetik, S. Gao, M. Wu, Z. Tang, D. Lin, D. Ding, W. Wu, Hybrid nanomanufacturing of mixed-dimensional manganese oxide/graphene aerogel macroporous hierarchy for ultralight efficient supercapacitor electrodes in self-powered ubiquitous nanosystems, *Nano Energy* 66 (2019) 104124.
- [44] P. Yan, E. Brown, Q. Su, J. Li, J. Wang, C. Xu, C. Zhou, D. Lin, 3D printing hierarchical silver nanowire aerogel with highly compressive resilience and tensile elongation through tunable poisson's ratio, *Small* 13 (38) (2017) 1701756.
- [45] Q. Zhang, F. Zhang, S.P. Medarametla, H. Li, C. Zhou, D. Lin, 3D printing of graphene aerogels, *Small* 12 (13) (2016) 1702–1708.
- [46] J. Sekhar, R. Trivedi, Solidification microstructure evolution in the presence of inert particles, *Mater. Sci. Eng. A* 147 (1) (1991) 9–21.
- [47] S.S. Peppin, M.G. Worster, J. Wettlaufer, Morphological instability in freezing colloidal suspensions, *Proc. Royal Soc. A: Mathe. Phys. Eng. Sci.* 463 (2079) (2007) 723–733.
- [48] S. Peppin, J. Elliott, M.G. Worster, Solidification of colloidal suspensions, *J. Fluid Mech.* 554 (2006) 147–166.
- [49] T. Waschkies, R. Oberacker, M. Hoffmann, Investigation of structure formation during freeze-casting from very slow to very fast solidification velocities, *Acta Mater.* 59 (13) (2011) 5135–5145.
- [50] B. Delattre, H. Bai, R.O. Ritchie, J. De Coninck, A.P. Tomsia, Unidirectional freezing of ceramic suspensions: in situ X-ray investigation of the effects of additives, *ACS Appl. Mater. Interfaces* 6 (1) (2014) 159–166.
- [51] S. Deville, J. Adrien, E. Maire, M. Scheel, M. Di Michiel, Time-lapse, three-dimensional in situ imaging of ice crystal growth in a colloidal silica suspension, *Acta Mater.* 61 (6) (2013) 2077–2086.
- [52] S. Deville, E. Maire, A. Lasalle, A. Bogner, C. Gauthier, J. Leloup, C. Guizard, In situ X-ray radiography and tomography observations of the solidification of aqueous alumina particle suspensions—part I: initial instants, *J. Am. Ceram. Soc.* 92 (11) (2009) 2489–2496.
- [53] S. Deville, E. Maire, A. Lasalle, A. Bogner, C. Gauthier, J. Leloup, C. Guizard, In situ X-ray radiography and tomography observations of the solidification of aqueous alumina particles suspensions. Part II: Steady State, *J. Am. Ceramic Soc.* 92 (11) (2009) 2497–2503.
- [54] S. Deville, E. Maire, G. Bernard-Granger, A. Lasalle, A. Bogner, C. Gauthier, J. Leloup, C. Guizard, Metastable and unstable cellular solidification of colloidal suspensions, *Nat. Mater.* 8 (12) (2009) 966–972.
- [55] N.P. Calta, J. Wang, A.M. Kiss, A.A. Martin, P.J. Depond, G.M. Guss, V. Thampy, A.Y. Fong, J.N. Weker, K.H. Stone, An instrument for in situ time-resolved X-ray imaging and diffraction of laser powder bed fusion additive manufacturing processes, *Rev. Sci. Instrum.* 89 (5) (2018) 055101.
- [56] A.A. Martin, N.P. Calta, S.A. Khairallah, J. Wang, P.J. Depond, A.Y. Fong, V. Thampy, G.M. Guss, A.M. Kiss, K.H. Stone, Dynamics of pore formation during laser powder bed fusion additive manufacturing, *Nat. Commun.* 10 (1) (2019) 1–10.
- [57] Q. Guo, C. Zhao, M. Qu, L. Xiong, S.M.H. Hojatzadeh, L.I. Escano, N.D. Parab, K. Fezzaa, T. Sun, L. Chen, In-situ full-field mapping of melt flow dynamics in laser metal additive manufacturing, *Addit. Manuf.* 31 (2020) 100939.
- [58] C. Zhao, K. Fezzaa, R.W. Cunningham, H. Wen, F. De Carlo, L. Chen, A.D. Rollett, T. Sun, Real-time monitoring of laser powder bed fusion process using high-speed X-ray imaging and diffraction, *Sci. Rep.* 7 (1) (2017) 1–11.
- [59] N.D. Parab, C. Zhao, R. Cunningham, L.I. Escano, K. Fezzaa, W. Everhart, A.D. Rollett, L. Chen, T. Sun, Ultrafast X-ray imaging of laser–metal additive manufacturing processes, *J. Synchrotron Radiat.* 25 (5) (2018) 1467–1477.
- [60] S.J. Wolff, H. Wu, N. Parab, C. Zhao, K.F. Ehmman, T. Sun, J. Cao, In-situ high-speed X-ray imaging of piezo-driven directed energy deposition additive manufacturing, *Sci. Rep.* 9 (1) (2019) 1–14.
- [61] N.D. Parab, J.E. Barnes, C. Zhao, R.W. Cunningham, K. Fezzaa, A.D. Rollett, T. Sun, Real time observation of binder jetting printing process using high-speed X-ray imaging, *Sci. Rep.* 9 (1) (2019) 1–10.
- [62] J. Sun, J. Ng, J. Fuh, Y. Wong, E. Thian, R. Yang, K.K. Tan, Fabrication of electronics devices with multi-material drop-on-demand dispensing system, 2010 International Conference on Manufacturing Automation, IEEE, 2010.
- [63] D. Rose, Microdispensing technologies in drug discovery, *Drug Discov. Today* 4 (9) (1999) 411–419.
- [64] C. Wang, R.I. Tomov, R.V. Kumar, B.A. Glowacki, Inkjet printing of gadolinium-doped ceria electrolyte on NiO-YSZ substrates for solid oxide fuel cell applications, *J. Mater. Sci.* 46 (21) (2011) 6889–6896.
- [65] C. Wang, S.C. Hopkins, R.I. Tomov, R.V. Kumar, B.A. Glowacki, Optimisation of CGO suspensions for inkjet-printed SOFC electrolytes, *J. Eur. Ceram. Soc.* 32 (10) (2012) 2317–2324.
- [66] L. Nayak, S. Mohanty, S.K. Nayak, A. Ramadoss, A review on inkjet printing of nanoparticle inks for flexible electronics, *J. Mater. Chem. C* 7 (29) (2019) 8771–8795.
- [67] B. Derby, Inkjet printing ceramics: from drops to solid, *J. Eur. Ceram. Soc.* 31 (14) (2011) 2543–2550.
- [68] G. Cummins, M.P. Desmulliez, Inkjet printing of conductive materials: a review, *Circuit World* (2012).
- [69] B. Derby, Inkjet printing of functional and structural materials: fluid property requirements, feature stability, and resolution, *Annu. Rev. Mater. Res.* 40 (2010) 395–414.
- [70] G. Kollamaram, S.C. Hopkins, B.A. Glowacki, D.M. Croker, G.M. Walker, Inkjet printing of paracetamol and indomethacin using electromagnetic technology: rheological compatibility and polymorphic selectivity, *Eur. J. Pharm. Sci.* 115 (2018) 248–257.
- [71] D.B. van Dam, C. Le Clerc, Experimental study of the impact of an ink-jet printed droplet on a solid substrate, *Phys. Fluids* 16 (9) (2004) 3403–3414.
- [72] O.R. Enríquez, Á.G. Marín, K.G. Winkels, J.H. Snoeijer, Freezing singularities in water drops, *Phys. Fluids* 24 (9) (2012) 091102.
- [73] A.G. Marin, O.R. Enríquez, P. Brunet, P. Colinet, J.H. Snoeijer, Universality of tip singularity formation in freezing water drops, *Phys. Rev. Lett.* 113 (5) (2014) 054301.
- [74] J.H. Snoeijer, P. Brunet, Pointy ice-drops: how water freezes into a singular shape, *Am. J. Phys.* 80 (9) (2012) 764–771.
- [75] J. Stringer, B. Derby, Formation and stability of lines produced by inkjet printing, *Langmuir* 26 (12) (2010) 10365–10372.
- [76] N. Mingirulli, R. Keding, J. Specht, A. Fallisch, D. Stüwe, D. Biro, Hot-melt inkjet as masking technology for back-contacted cells, 2009 34th IEEE Photovoltaic Specialists Conference (PVSC), IEEE, 2009.
- [77] V. Sukhotskiy, I. Karampelas, G. Garg, A. Verma, M. Tong, S. Vader, Z. Vader, E. Furlani, Magnetohydrodynamic drop-on-demand liquid metal 3D printing, *Solid Freeform Fabr. Symp. Proc.* (2017).